

Semester Thesis

Simulation of Aerodynamic Tails for ANYmal

Case Study: Cheetah

Autumn Term 2024

Declaration of Originality

I hereby declare that the written work I have submitted entitled

Your Project Title

is original work which I alone have authored and which is written in my own words.¹

Author(s)

Max Greiner

Student supervisor(s)

Robert Baines
Yuntao Ma
Ardian Jusufi

Supervising lecturer

Marco Hutter

With the signature I declare that I have been informed regarding normal academic citation rules and that I have read and understood the information on 'Citation etiquette' (<https://www.ethz.ch/content/dam/ethz/main/education/rechtliches-abschluesse/leistungskontrollen/plagiarism-citationetiquette.pdf>). The citation conventions usual to the discipline in question here have been respected.

The above written work may be tested electronically for plagiarism.

Adetsw.l

14.10.2024

Place and date



Signature

¹Co-authored work: The signatures of all authors are required. Each signature attests to the originality of the entire piece of written work in its final form.

Intellectual Property Agreement

The student acted under the supervision of Prof. Hutter and contributed to research of his group. Research results of students outside the scope of an employment contract with ETH Zurich belong to the students themselves. The results of the student within the present thesis shall be exploited by ETH Zurich, possibly together with results of other contributors in the same field. To facilitate and to enable a common exploitation of all combined research results, the student hereby assigns his rights to the research results to ETH Zurich. In exchange, the student shall be treated like an employee of ETH Zurich with respect to any income generated due to the research results.

This agreement regulates the rights to the created research results.

1. Intellectual Property Rights

1. The student assigns his/her rights to the research results, including inventions and works protected by copyright, but not including his moral rights ("Urheberpersönlichkeitsrechte"), to ETH Zurich. Herewith, he cedes, in particular, all rights for commercial exploitations of research results to ETH Zurich. He is doing this voluntarily and with full awareness, in order to facilitate the commercial exploitation of the created Research Results. The student's moral rights ("Urheberpersönlichkeitsrechte") shall not be affected by this assignment.
2. In exchange, the student will be compensated by ETH Zurich in the case of income through the commercial exploitation of research results. Compensation will be made as if the student was an employee of ETH Zurich and according to the guidelines "Richtlinien für die wirtschaftliche Verwertung von Forschungsergebnissen der ETH Zürich".
3. The student agrees to keep all research results confidential. This obligation to confidentiality shall persist until he or she is informed by ETH Zurich that the intellectual property rights to the research results have been protected through patent applications or other adequate measures or that no protection is sought, but not longer than 12 months after the collaborator has signed this agreement.
4. If a patent application is filed for an invention based on the research results, the student will duly provide all necessary signatures. He/she also agrees to be available whenever his aid is necessary in the course of the patent application process, e.g. to respond to questions of patent examiners or the like.

2. Settlement of Disagreements

Should disagreements arise out between the parties, the parties will make an effort to settle them between them in good faith. In case of failure of these agreements, Swiss Law shall be applied and the Courts of Zurich shall have exclusive jurisdiction.

Adhswil

14.10.2024

Place and date



Signature

Contents

Preface	v
Abstract	vii
Symbols	ix
1 Introduction	1
2 Methods	3
2.1 Robot and Drag Model	3
2.2 Calculating Drag Force Analytically	4
2.3 Force Fields	8
2.4 Simulation	9
2.4.1 Tail Joint Control	9
2.4.2 Track Joint Control	10
2.4.3 Accessing the roll torque	10
2.4.4 Force Field Configuration	10
3 Results	13
3.1 Comparison of Analytical and ForceField Approach	13
3.2 Effect of Hunting Speed on the Angular Impulse	15
4 Conclusion	17
5 Outlook	18
Bibliography	19
A Projected Surface Area	21
B Angular Velocity Tracking	23

Preface

In the scope of this project I was challenged to use the Nvidia Isaac Sim and Isaac Lab simulation software. For someone that has never worked with simulations before or on a large code base like this, it was at times definitely overwhelming. I would like to thank Mayank Mittal specifically for his help at the 11th hour of my patience, to overcome the last hurdles to get the simulation working. Aside from his specific technical support, a special thanks goes to

Robert Baines for kind words, the consideration and patience to listen to my lengthy not-progress-reports week by week.

Yuntao Ma for his intuition on rephrasing math problems and out-of-the-box thinking.

Ardian Yusufi for the continuous flow of biomechanical examples, motivating the relevance of this project.

I look back at this project remembering all the frustrating debugging sessions as well as the extremely hectic phase when closing in on the deadline. In the end, aren't the unpleasant experiences the most memorable?

I am fortunate to have had the opportunity to work on this project and appreciate the faith placed in me to tackle this first step into the (partially) unknown realm of aerodynamic drag simulation using Isaac Sim.

Abstract

This project introduces two methods to simulate aerodynamic drag in the Nvidia Isaac Sim / Isaac Lab [1] framework. The long term motivation is to evaluate the viability and explore the design space of robotic tails, making use of aerodynamic forces.

The case study used for this project refers to the open question in biomechanics on how large the aerodynamic contribution to the roll torque in a hunting cheetah is. Two different methods for simulating aerodynamic drag are presented. An analytical method, specific to the case study, is derived and implemented. This method is compared to the Nvidia Omniverse Force Fields extension [2].

The analytical approach taken is specific to this case study, hence not generally applicable. Contrary to this, the force fields approach is "plug and play" and generalizes to any arbitrary rigid body model in the simulation environment. The force fields approach simulates forces and not drag induced by wind directly. Because of this, the robot model is required to move through space to simulate incoming wind, which may not be feasible for robot models requiring ground contact.

All in all, the force field extension has the major benefit of being generally applicable to any multi DoF robot.

The evaluation of the case study shows that aerodynamic drag contributes 7.17% of the total angular impulse for a hunting speed of 30 m/s. At lower hunting speeds, the aerodynamic contribution quickly drops below 3%, despite using the same tail velocity profile for all tested hunting speeds.

The source code to this project can be found on GitHub [LINK].

Symbols

Symbols

ρ	Density of air at 1.225kg/m ³
C_D, C_{Drag}	Drag coefficient
$A_{\perp v}, A_{\perp}$	Projected surface area onto plane perpendicular to v
$\mathbf{a} \times \mathbf{b}$	Cross product between two vectors

Indices

x	x axis
y	y axis
z	z axis
Tail, T	Subscript for tail
Wind, W	Subscript for wind, meaning the incoming wind
$\mathbf{e}_i, \mathbf{e}_i$	Unit vector for some quantity i or 'i'
A_{Δ}	Delta as subscript is used to denote an infinitesimal quantity of any value A

Acronyms and Abbreviations

DoF	Degrees of Freedom
CoM	Center of Mass
PD	Proportional-Derivative, a type of controller structure
ETH	Eidgenössische Technische Hochschule

Chapter 1

Introduction

In recent years, the research community has gained interest in analyzing how tails enhance maneuverability in animals. Some examples include air-righting in arboreal geckos where the tail provides torques through inertia and aerodynamic forces to adjust its attitude in mid-air [3]. Another famous example includes the cheetah's tail, which exhibits distinct trajectories during deceleration or change of direction [4]. The observed tail motion has undoubtedly an impact on stability during high-speed chases. However, it is not yet clear on how this contribution is split between (1) inertial effects, due to the tail's length, mass and acceleration, or (2) aerodynamic drag effects, due to the high experienced wind speeds.

In robotics, we often take inspiration from nature, for which reason different bio-inspired robotic tails have been developed in recent years [5][6][7]. To optimize the robotic counterpart, a deep understanding of how biological tails function is required. For this, we refer back to the question of the cheetah's tail, where it is unclear how much the aerodynamic drag contributes to the tail's stabilizing torque on the body.

This work uses the Isaac Sim simulation platform by Nvidia [1] to implement and evaluate a framework for aerodynamic tail simulation. As a case study, the question about how aerodynamic forces contribute to the roll torque in cheetahs is analyzed.

Chapter 2 covers the aerodynamic and robot model used to discuss the case study. Then, two different methods on implementing aerodynamic drag forces into the simulation software are discussed. The final part of this chapter section 2.4 discusses some simulation specific considerations about controlling the robot model.

In chapter 3, first a comparison on the two different aerodynamic simulation methods is made. Following the aerodynamic roll torque contribution in cheetahs dependent on hunting speed is analyzed.

Finally, chapter 4 concludes the results while chapter 5 provides an outlook.

Chapter 2

Methods

While this thesis aims to implement a generic and scalable approach to simulate tails with aerodynamic forces, the setup described in section 2.1 is used for this case study, simulating a cheetah tail-flick at high speeds. Any comparisons made are based off the question from the introduction; what is the roll torque composition between aerodynamic and inertial effects induced by a tail-flick motion at high hunting speeds.

Two different methods to incorporate aerodynamic effects in simulation are implemented, compared and discussed. The first method in 2.2 derives the drag force based on the tail position and velocity and applies a substituting force through the tail's center of mass (CoM). This approach is called "the analytical approach". The second method in section 2.3 uses an Omniverse plugin called 'Force Fields' [2], which as the name suggests offers methods to apply drag-like (and other) forces on rigid bodies. For a detailed look at the implementation of the simulation the reader is referred to the GitHub page .

The last section of this chapter 2.4 elaborates on design choices for controlling the robot model in simulation.

2.1 Robot and Drag Model

The simplified model depicted in fig. 2.1 is sufficient to consider the case study, which deals with the roll torque induced through a rotation of the tail about the roll axis. In particular, the aerodynamic compared to the inertial contribution of the roll torque from a fast tail-flicking motion, as observed during high speed cheetah chases [8], is analyzed.

Parallel to this work, Felix Winghart is in the final stages of performing wind tunnel experiments of a setup analogous to the one introduced here.

Figure 2.1 shows the robot model used throughout this project. The cheetah body is modelled as a simple rigid cube, where the tail is approximated as a 1 degree of freedom (DoF) rigid rod which can rotate about the roll axis. The incoming wind, simulating a running cheetah, acts along the roll axis.

The drag model used is inspired by work from Patel et al. [4]. The drag model is shown in 2.1, where $A_{\perp \mathbf{v}}$ is the surface area *perpendicular* to the wind velocity \mathbf{v} . The constants C_{Drag} and ρ are drag coefficient and density of air respectively. Equation 2.1 is a vector equation, where $\mathbf{e}_{\mathbf{v}}$ represents the unit vector of \mathbf{v} .

$$\mathbf{F}_{\text{Drag}} = \frac{1}{2} \rho A_{\perp \mathbf{v}} C_{\text{Drag}} \mathbf{e}_{\mathbf{v}} \|\mathbf{v}\|^2 \quad (2.1)$$

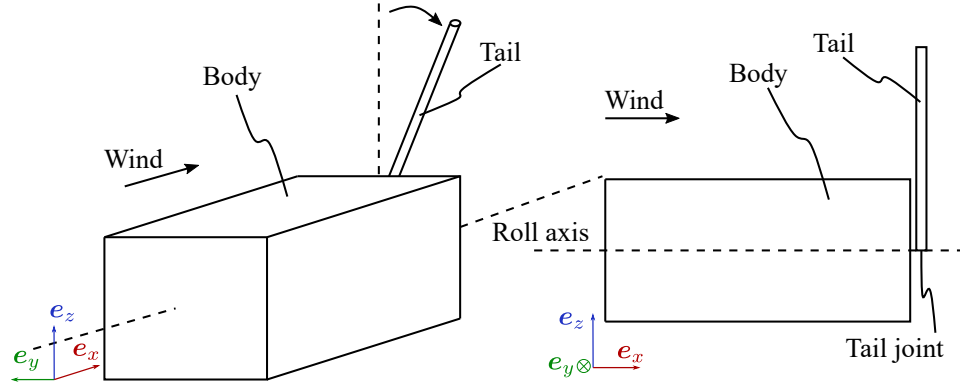


Figure 2.1: This figure shows the model used to tackle the case study of the roll torque in a hunting cheetah. Left is a 3D sketch, on the right is a side view. Attached to the robot body is a tail, approximated as a rigid rod, which can rotate about the roll axis only. The incoming wind acts along the roll axis.

2.2 Calculating Drag Force Analytically

The first method discussed takes an analytical approach to calculating the total drag force acting on the tail and applying a substitution force through the tail's center of mass (CoM), resulting in an equivalent torque about the tail's joint.

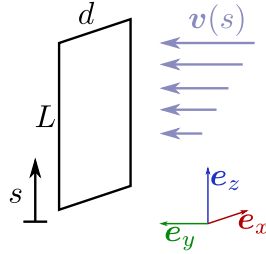


Figure 2.2: A surface $A = L \cdot d$ experiences a perpendicular velocity field $v(s)$.

First, we introduce the notion of an infinitesimal surface area, A_Δ , as it will be used later. Take the setup described in fig. 2.2 where a wind field is described by $\mathbf{v}(s)$, acting *perpendicular* to a surface area $A = Ld$. The infinitesimal drag force is calculated using the drag equation 2.1 with A being the infinitesimal surface area A_Δ and the wind acting on this infinitesimal area $\mathbf{v}(s)$. Equation 2.2 shows the formula using vector notation, where $\mathbf{v}(s)$ is the wind vector and $\mathbf{e}_{\mathbf{v}(s)}$ is the unitary direction vector of the wind at position s .

To find A_Δ we know that $\int_0^L A_\Delta ds \equiv Ld$, from which $A_\Delta = d$ can be concluded. Using the drag formula introduced in eq. (2.1), eq. (2.2) summarizes the infinitesimal drag force $\mathbf{F}_{\Delta\text{Drag}}(s)$ and integrates that to the total drag force \mathbf{F}_{Drag} .

$$\begin{aligned} \mathbf{F}_{\Delta\text{Drag}}(s) &= \frac{1}{2} \rho \underbrace{A_\Delta}_d C_D \mathbf{e}_{\mathbf{v}(s)} \|\mathbf{v}(s)\|^2 \\ \mathbf{F}_{\text{Drag}} &= \int_0^L \frac{1}{2} \rho d C_D \mathbf{e}_{\mathbf{v}(s)} \|\mathbf{v}(s)\|^2 ds \end{aligned} \quad (2.2)$$

For the setup described in fig. 2.1 there are two factors, determining the total wind velocity perceived by any point along the tail. The incoming wind, \mathbf{v}_{Wind} , and the wind introduced by rotation of the tail about the roll axis, \mathbf{v}_{Rot} .

Figure 2.3 shows our setup from a side and top view. The incoming wind, simulating a high-speed cheetah chase, is denoted by \mathbf{v}_{Wind} and acts along the roll axis. The tail, perpendicular to the incoming wind \mathbf{v}_{Wind} , can rotate about the tail joint. The angular velocity is given by $\|\boldsymbol{\omega}\|$ and the direction by \mathbf{e}_{ω} , according to the right-hand rule. Rotation about the axis $\boldsymbol{\omega}$ in turn results in a velocity \mathbf{v}_{Tail} of the tail itself, which leads to an opposing wind vector \mathbf{v}_{Rot} . The vector \mathbf{v}_{Rot} denotes the wind perceived by a fixed point on the tail. Finally, $\mathbf{x}(s)$ is introduced in eq. (2.3) as a vector starting at the tail joint pointing outwards along the tail, defined for $s \in [0, L]$, where L denotes the length of the tail and $\mathbf{e}_{\text{dir}(\mathbf{x})}$ is a unit vector pointing outwards from the joint along the tail, providing the direction.

$$\mathbf{x}(s) = s \mathbf{e}_{\text{dir}(\mathbf{x})}, \forall s \in [0, L] \quad (2.3)$$

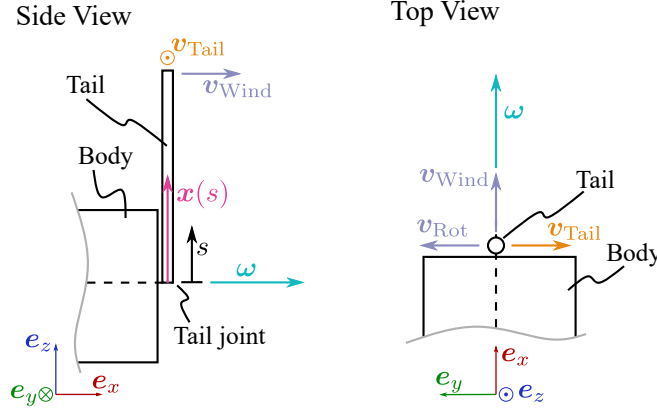


Figure 2.3: This figure provides a side and top view of the robot model, with respective wind and rotational velocities denoted. The tail can rotate about the tail joint according to the right hand rule and the defined rotation axis $\boldsymbol{\omega}$. The vector $\mathbf{x}(s)$ starts at the tail joint and points outwards along the tail, defined for $s \in [0, L]$, with L being the total tail length.

The rotational wind component \mathbf{v}_{Rot} can be expressed by the cross product of $\boldsymbol{\omega}$ with $\mathbf{x}(s)$, as shown in eq. (2.4).

$$\mathbf{v}_{\text{Rot}}(s) = -\mathbf{v}_{\text{Tail}}(s) = -(\boldsymbol{\omega} \times \mathbf{x}(s)) \quad (2.4)$$

The total wind velocity experienced along a point s on the tail can be expressed through the sum of \mathbf{v}_{Wind} with \mathbf{v}_{Rot} . Equation 2.5 shows the sum of the two wind components and simplifies using the expression from eq. (2.4).

$$\begin{aligned} \mathbf{v}(s) &= \mathbf{v}_{\text{Wind}} + \mathbf{v}_{\text{Rot}}(s) \\ \mathbf{v}(s) &= \mathbf{v}_{\text{Wind}} - \underbrace{(\boldsymbol{\omega} \times \mathbf{x}(s))}_{\mathbf{v}_{\text{Tail}}} \end{aligned} \quad (2.5)$$

The drag model eq. (2.1) requires any surface area to be projected onto a plane perpendicular to the incoming wind $\mathbf{v}(s)$, where the projected surface area is denoted by A_{\perp} . For the setup discussed here, $\mathbf{x}(s)$, \mathbf{v}_{Rot} and \mathbf{v}_{Wind} provide an orthogonal basis (refer to fig. 2.3). The total wind experienced anywhere along the tail, expressed by eq. (2.5), will not leave the plane spanned by the two vectors \mathbf{v}_{Wind} and

\mathbf{v}_{Rot} . Hence, any total perceived wind along the tail $\mathbf{v}(s)$ will always be perpendicular to $\mathbf{x}(s)$. Because of this, the projected surface area for the simplified case in this project is given by $A_{\perp \mathbf{v}(s)} = A = Ld$, where L denotes the tail length and d the diameter.

For the general case however, the longitudinal axis of the cylindrical tail ($\mathbf{x}(s)$) must be projected accordingly to get $A_{\perp \mathbf{v}(s)} = L_{\text{proj}}d$. Given the simplification for the case study, where \mathbf{v}_{Wind} acts perfectly in line with the roll axis, the calculation of L_{proj} is not strictly necessary.

For brevity, the notion of L_{proj} is introduced as a general way to calculate $A_{\perp \mathbf{v}}$, but only explained in appendix A further.

With L_{proj} the projected surface area is given by $A_{\perp \mathbf{v}(s)} = L_{\text{proj}}d$. The infinitesimal surface area A_{Δ} is then derived, knowing that the integration of A_{Δ} over s must provide $A_{\perp \mathbf{v}(s)}$ in turn, which is shown in eq. (2.6).

As previously explained, $L_{\text{proj}} \equiv L$ given the orthogonal basis by $\mathbf{x}(s)$, \mathbf{v}_{Rot} and \mathbf{v}_{Wind} for any tail position for the case study discussed. Hence, the notion of projected length is not strictly necessary for this work but elaborated in appendix A for sake completeness and generality.

$$\begin{aligned} A_{\perp \mathbf{v}(s)} &= L_{\text{proj}} d \\ A_{\perp \mathbf{v}(s)} &= \int_0^L A_{\Delta} ds = \int_0^L \underbrace{\left(\frac{L_{\text{proj}}}{L} d \right)}_{A_{\Delta}} s ds \end{aligned} \quad (2.6)$$

Given the expressed quantities from eq. (2.5) and eq. (2.6), eq. (2.2) can be used to calculate $\mathbf{F}_{\Delta \text{Drag}}$ and \mathbf{F}_{Drag} .

The total torque $\mathbf{T}_{\text{total}}$ at the tail joint due to aerodynamic drag can be expressed as an integral over the cross product of $\mathbf{x}(s)$ with $\mathbf{F}_{\Delta \text{Drag}}$, as shown in eq. (2.7).

$$\mathbf{T}_{\text{total}} = \int_0^L \mathbf{x}(s) \times \mathbf{F}_{\Delta \text{Drag}}(s) ds \quad (2.7)$$

To implement this into the simulation framework, a substitution force \mathbf{F}_{sub} acting through the tail's CoM, leading to the same total torque $\mathbf{T}_{\text{Total}}$ (eq. (2.7)) is required.

$$\mathbf{x}(s) \times \mathbf{F}_{\text{sub}} = \mathbf{T}_{\text{total}} \quad (2.8)$$

Solving eq. (2.8) for \mathbf{F}_{sub} however is not trivial without any assumptions on the direction of \mathbf{F}_{sub} .

The direction of the substitution force must lie in the plane spanned by \mathbf{v}_{Wind} and \mathbf{v}_{Rot} . This can be argued because any drag force opposes the direction of the total wind $\mathbf{v}(s)$, which according to eq. (2.5) must lie in the plane spanned by \mathbf{v}_{Wind} and \mathbf{v}_{Rot} .

With this constraint in mind, there must exist some α and β such that $\mathbf{F}_{\text{sub}} = \alpha \mathbf{v}_{\text{Wind}} + \beta \mathbf{v}_{\text{Rot}}$, which helps to simplify expression expression 2.9. The eq. (2.9) is now rephrased in terms of α and β .

$$\begin{aligned}
& \mathbf{x}(s) \times \mathbf{F}_{\text{sub}} = \mathbf{T}_{\text{total}} \\
& \mathbf{x}(s) \times \underbrace{\left(\alpha \mathbf{v}_{\text{Wind}} + \beta \mathbf{v}_{\text{Rot}}(s) \right)}_{\mathbf{F}_{\text{sub}}} = \mathbf{T}_{\text{total}} \\
& \alpha \left(\mathbf{x}(s) \times \mathbf{v}_{\text{Wind}} \right) + \beta \left(\mathbf{x}(s) \times \mathbf{v}_{\text{Rot}}(s) \right) = \mathbf{T}_{\text{total}} \\
& \begin{bmatrix} \mathbf{x}(s) \times \mathbf{v}_{\text{Wind}} & \mathbf{x}(s) \times \mathbf{v}_{\text{Rot}}(s) \end{bmatrix} \cdot \begin{bmatrix} \alpha \\ \beta \end{bmatrix} = \mathbf{T}_{\text{total}}
\end{aligned} \tag{2.9}$$

Solving for α and β requires some additional care, as $\|\mathbf{v}_{\text{Wind}}\|$ or $\|\mathbf{v}_{\text{Rot}}\|$ can be zero, depending on the simulation configuration (e.g. incoming wind is disabled or $\|\boldsymbol{\omega}\|$ is zero). In each case, the respective scaling factor (α or β) must be set to zero to maintain a unique solution for \mathbf{F}_{sub} in accordance to eq. (2.10).

$$\mathbf{F}_{\text{sub}} = \alpha \mathbf{v}_{\text{Wind}} + \beta \mathbf{v}_{\text{Rot}} \tag{2.10}$$

The substitution force can then be applied at each time step in the simulation using the function `articulation.set_external_force_and_torque()` to the tail's CoM.

2.3 Force Fields

Isaac Sim has an extension called "Force Fields" which offers tools for simulating differently parametrized forces onto rigid bodies in the simulation environment [2]. For this project, the "Drag Force Field" was used which applies an opposing force relative to a rigid object's velocity. Only the tail is exposed to this force field.

To simulate the incoming wind \mathbf{v}_{Wind} , the setup as described in section 2.1 is moved through space using a prismatic joint. As a visual aid, a track is added to the simulation to show at a glance how the robot can move through space.

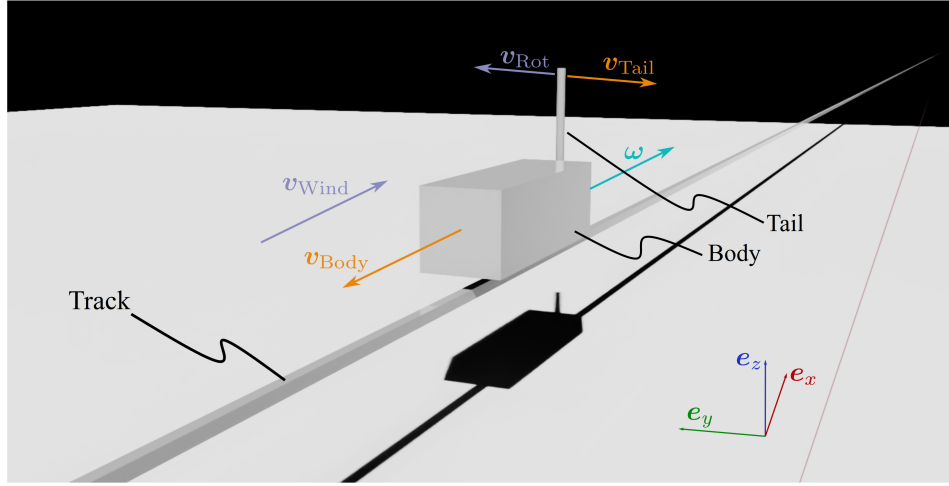


Figure 2.4: Robot model with a prismatic joint allowing motion in \mathbf{e}_x direction along the track. By controlling the track joint (details in section 2.4.2) the body moves through space along \mathbf{v}_{Body} while experiencing incoming wind \mathbf{v}_{Wind} . Additionally, the tail is actuated and moves around the roll axis of the robot along \mathbf{v}_{Tail} . Collision for the track is disabled, e.g. the tail swings through the track as if it were not present.

Because the force fields extension allows to use multiple force fields, it would be intuitive to use two force fields; (1) a drag force field (2) and a planar (or wind) force field. Despite not having tested this rigorously, we do not expect a combination of force fields to achieve a correct simulation result. To show this, I refer to the figure 2.3 which shows a top down view of a cylinder.

Assume the wind comes from the front (shown is a top down vie), depicted with \mathbf{v}_{Wind} . The cylinder is moved to the right, which results in a perceived wind direction according to $\mathbf{v}_{\text{Perceived}}$. Adding the two velocities together gives $\mathbf{v}_{\text{Total}}$. For each of the three velocity vectors, we can derive a drag force which is proportional to it's respective velocity using $\|\mathbf{F}_i\| \propto \|\mathbf{v}_i\|^2$. The forces $\mathbf{F}_1(\mathbf{v}_{\text{Wind}})$, $\mathbf{F}_2(\mathbf{v}_{\text{Perceived}})$, $\mathbf{F}_3(\mathbf{v}_{\text{Total}})$ are depicted in the figure as well. It is easy to show, that $\mathbf{F}_3 \neq \mathbf{F}_1 + \mathbf{F}_2$. The true drag force acting should be $\|\mathbf{F}_3\| \propto \|\mathbf{v}_{\text{Total}}\|^2$.

Using two different force fields would lead to the synonymous $\mathbf{F}_{\text{ForceField1}} + \mathbf{F}_{\text{ForceField2}}$ type of approach, which is incorrect when simulating the drag force stemming from two different wind components \mathbf{v}_{Wind} and $\mathbf{v}_{\text{Perceived}}$.

Hence, only the drag force field is used and the robot base is moved through the simulation environment to simulate the incoming wind while the tail rotates.

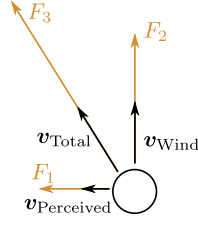


Figure 2.5: Top down view of a cylinder on which incoming wind \mathbf{v}_{Wind} is acting from the bottom, while the cylinder is moved to the right experiencing $\mathbf{v}_{\text{Perceived}}$. Each \mathbf{F}_i represents the drag force calculated according to $\|\mathbf{F}_i\| \propto \|\mathbf{v}_i\|^2$. It is clear that if $\|\mathbf{F}_3\| \propto \|\mathbf{v}_{\text{Total}}\|^2$, that in the general case $\|\mathbf{F}_3\| \neq \|\mathbf{F}_1 + \mathbf{F}_2\| \propto \|\mathbf{v}_{\text{Perceived}}\|^2 + \|\mathbf{v}_{\text{Wind}}\|^2$. Sketch is not to scale.

2.4 Simulation

To simulate the robot, a control policy is required. This section discusses the considerations made to achieve reasonable simulation results. The precise simulation parameters chosen can be taken from the source code on GitHub or found in chapter 3.

2.4.1 Tail Joint Control

The simulation environment supports three different control schemes; position, velocity and torque/force. All of these schemes are controlled by an underlying proportional-derivative (PD) controller, where joint stiffness represents the p-gain and the joint damping by the d-gain.

For all results shown in chapter 3 velocity control is used with a joint damping value of 5 and zero stiffness. Velocity control is chosen because we assume the tail-flick of a cheetah to entail a (somewhat) linear acceleration phase which then flattens when reaching the upper velocity limit of 20 rad/s [7]. The acceleration rate used of 100 rad/s^2 is an educated guess on the basis that the tail flick might happen in a time span of approximately 0.2s. The velocity setpoint curve is shown in fig. 2.6. In order to have a reasonable tracking behavior, the damping value of 5 is chosen on experimental basis such that the velocity profile shows continuous behavior around 0s and 0.2s.

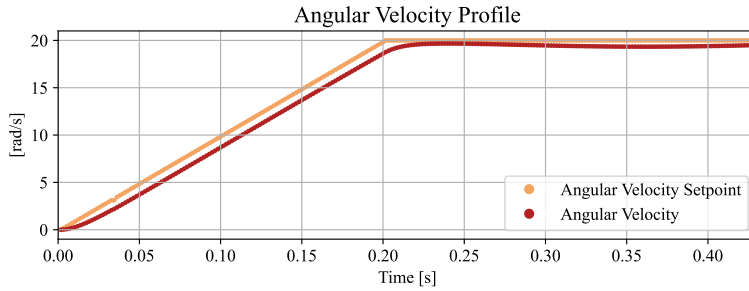


Figure 2.6: In orange the angular velocity setpoint, characterized by an acceleration rate of 100 rad/s^2 and a maximum velocity of 20 rad/s . In red the tracked velocity profile where the tail joint damping is set to 5 and stiffness to zero.

Because the tracking behavior between different simulation parameters can deviate slightly, statistics on the angular velocities can be found in appendix B. These statistics are provided for sake of completeness as it is fundamental to verify that the tail motion is indeed similar between simulation runs, before comparing induced roll torques.

These differences are shown to be extremely minimal, to the point where the difference would not be visible if multiple different curves were shown in fig. 2.6. Going forward, only *one* tail joint velocity curve will be shown in the figures.

2.4.2 Track Joint Control

For simulations with the force fields extension, the base of the robot must move through space to simulate the incoming wind. It is important that the velocity setpoint is tracked precisely and continuously. To this end, a track joint damping value of 10^5 is chosen. This high damping value provides (nearly) instant and perfect tracking of the velocity setpoint. Statistics on how well the velocity setpoint is tracked is omitted, as the tracking error after one simulation step drops to values of magnitude 10^{-3} . Hence, it is accurate enough.

2.4.3 Accessing the roll torque

The Nvidia simulation framework provides a method to acquire measured joint forces and torques. For the floating base system (using omniverse Force Field extension) we measure the torque about the prismatic joint. In the analytical approach, since a fixed base model is used, the torque about the fixed joint at the CoM of the robot body is measured.

The python function used is `articulation.get_measured_joint_forces`.

2.4.4 Force Field Configuration

The force fields extension offers a drag force field which applies a force opposing the velocity of the rigid body in question. Some parameters require attention;

Surface Sample Density defines how many rays are cast for a 1 m by 1 m surface area. If this were zero, then no rotational moments are induced on rigid bodies as the substituting force would always act through the CoM. The value used for this project is 10^6 .

Surface Area Scale Enabled ensures that the infinitesimal force is scaled by the surface area.

Square represents the coefficients leading the velocity-square term, e.g. $\frac{1}{2}\rho C_D = 0.735 \text{ kg/m}^3$ with the values used in this analysis.

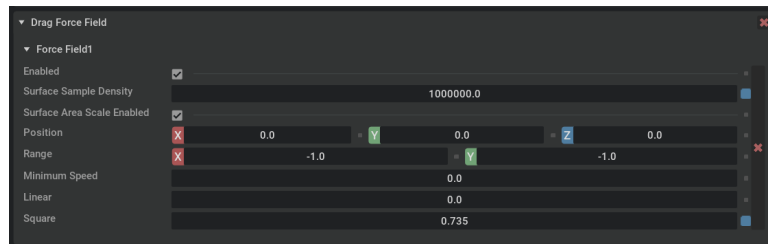


Figure 2.7: Screenshot from the Isaac Sim UI of the configuration parameters for the drag force field.

Chapter 3

Results

All results presented make use of the model introduced in section 2.1. The case study discussed deals with the roll torque in a hunting cheetah scenario, which is comprised of aerodynamic and inertial effects.

Cheetah specific parameters stem mostly from Patel et al. [4]. Their work includes valuable assumptions, simulations and measurements on real cheetah tails.

Tail parameters like length (0.7 m), diameter (0.05 m) and mass (0.7 kg), as well as the drag coefficient ($C_D = 1.2$), torque limit (30 Nm) are all chosen on the basis of Patel et al. [4]. The choice for the incoming wind velocity, simulating hunting conditions, is chosen to be 30 m/s [4][7]. Finally, the average tail flick speed observed in cheetahs comes from P.Hudson et al., cited and used by Patel et al. [4], at $17 \pm 4 \text{ rad/s}$. Because of this, the tail joint velocity profile from section 2.4.1 is characterized to have a maximum velocity of 20 rad/s .

3.1 Comparison of Analytical and ForceField Approach

To compare the analytical implementation with the drag force field extension [2], both methods are simulated twice; once with aerodynamic and once without aerodynamic forces enabled. The tail joint is controlled as described in 2.4.1, using the same velocity setpoint profile. Given the nature of the underlying controller, slight differences in effectively tracked velocity occurs between the individual simulations. For details on the difference between tracked angular tail velocities, please view the appendix B.

Figure 3.1 shows the angular velocity profile, including tail orientation in radians at the top, and multiple roll torque curves at the bottom. For each method, the analytical and force field method, two roll torque curves are shown in the bottom part of the figure. In hues of blue, the total roll torque, and in hues of green, the torque induced by aerodynamic forces are shown.

At 0.2s the angular velocity setpoint has a discontinuity, for which reason the underlying controller adjusts the torque in a discontinuous matter, hence the instant reduction in total torque (blue curves respectively). Ignoring the short initial transient phase, the total torque during the linear acceleration period up to 0.2 s remains fairly constant.

Because the aerodynamic contribution scales with the tail's joint velocity squared, we expect an increase from the aerodynamic contribution as the tail's rotation speed

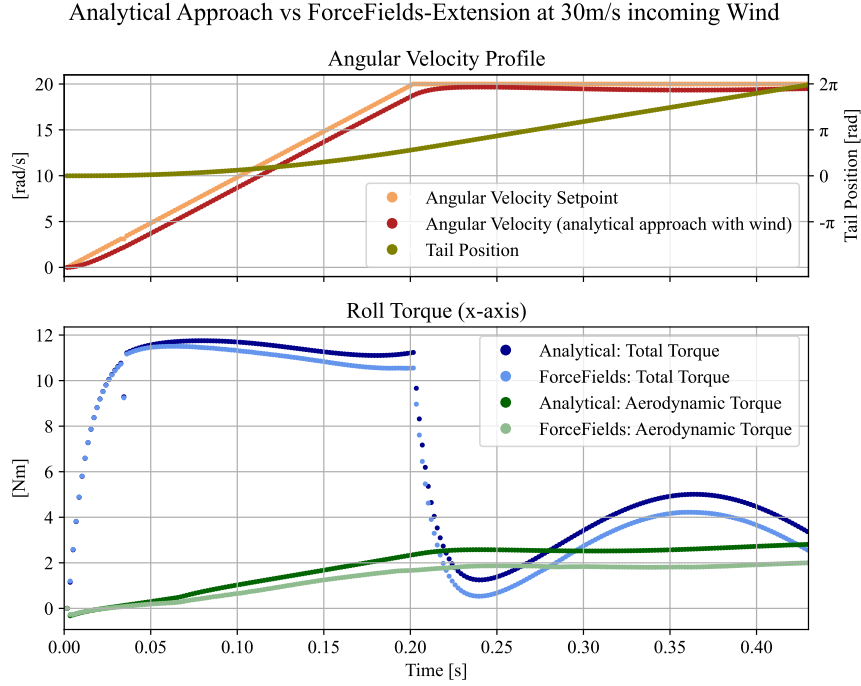


Figure 3.1: Top: Angular velocity setpoint of the tail, the measured angular velocity as well as the tail's position in radians. Bottom: In hues of blue the total roll torque in hues of green the aerodynamic roll torque contribution. The discontinuity at 0.2 s comes from the change in angular velocity setpoint.

increases. The seemingly linear increase and then constant contribution is clearly shown in hues of green.

The phase following 0.2 s is characterized by a sinus-shaped total torque profile. This pattern is in line with the frequency of the tail rotation and is due to the gravitational force periodically influencing the torque required to maintain a constant angular velocity.

The plot does not explicitly show, but it is mentioned here for completeness; the gap seen between the two total torque curves is exactly the same gap as seen between the two aerodynamic curves. This equivalence in difference validates that simulation of the inertia is indeed identical between the two approaches, hence the only difference lies in the simulation of aerodynamic drag forces.

Across both implementations the results show similar behavior across the entire time span, only difference being the magnitude of the aerodynamic contribution.

From the curves shown in fig. 3.1, the angular impulse, i.e. the integration of torque over time, can be calculated. Patel et al. [4] demonstrate that by reducing the aerodynamic contribution down to a single number (angular impulse), that it can be compared easily.

Table 3.1 shows the total angular impulse as well as the inertial and aerodynamic contribution. The last column provides the aerodynamic contribution in percentage of the total angular impulse. The angular impulse is calculated for $t \in [0 \text{ s}, 0.2 \text{ s}]$.

Patel et al. [4] have shown by simulation an aerodynamic angular impulse contri-

Table 3.1: Angular Impulse for $t \in [0\text{ s}, 0.2\text{ s}]$

Approach	Total Impulse [Nms]	Inertial Contr. [Nms]	Aerod. Contr. [Nms]	Aerod. Contr. (%)
Analytical	2.12	1.92	0.20	10.27%
ForceFields	2.06	1.92	0.14	7.17%
Patel et al. [4]	-	-	-	12.6%

Table 3.2: The angular impulse from fig. 3.1 is calculated for the analytical and force fields approach for the simulation duration of $t \in [0\text{ s}, 0.2\text{ s}]$. The total angular impulse is split into an inertial and a aerodynamic contribution. The aerodynamic contribution (Aerod. Contr.) is given in percentage as well. For reference, the aerodynamic angular impulse for the roll axis can reach up to 12.6%, according to Patel et al. [4].

bution of up to 12.6% for the roll axis in hunting cheetahs.

Comparing to the values from section 3.1, the analytical solution is closer to Patel's findings. However, Patel et al. [4] had used a slightly different control policy; instead of following a velocity profile, a torque profile starting at 30 Nm is applied until a 90° rotation of the tail was observed. The detailed torque control policy, which includes estimated power limits of the cheetah, can be found in his work. In the simulation results from this study the tail reaches 90° coincidentally at around 0.2 s, which is the limit used for the angular impulse calculation.

All in all, without knowing how the force fields are implemented or validating with experimental data, it is impossible to tell which of the two implemented approaches is more accurate. The fact that the aerodynamic torque contribution is in the same ballpark as the work done by Patel et al. [4] supports the results shown. Considering scalability of either approach, the force field extension clearly has the advantage to work out of the box for a diverse set of rigid bodies. The analytical approach is tailored to the case study in question, which limits generalization to other models. The only apparent limitation of the force field approach is the inability to simulate incoming winds without moving the base of the robot through space. For a robot model that requires ground contact, this method of simulating incoming winds becomes infeasible.

3.2 Effect of Hunting Speed on the Angular Impulse

Using the force fields implementation and the same angular velocity profile as discussed in section 2.4.1, multiple simulations are run for varying incoming wind speeds, simulating different hunting velocities. For each wind speed the simulation is run once with and once without the incoming wind.

For details on the precise angular velocities of the tail and how they relate to each other across the simulation runs, please refer to the appendix B.

Figure 3.2 shows the tail parameters (velocity, setpoint and position) in the top figure and a bar plot in the bottom figure. Each bar represents one specific incoming wind velocity. The aerodynamic angular impulse component is in blue and annotated with the percentage of total angular impulse. In green is the inertial angular impulse component. The angular impulse is calculated for $t \in [0\text{ s}, 0.2\text{ s}]$.

As the incoming wind component (perpendicular to the tail's rotation plane, refer to section 2.1) increases for a given tail velocity profile, the aerodynamic contribu-

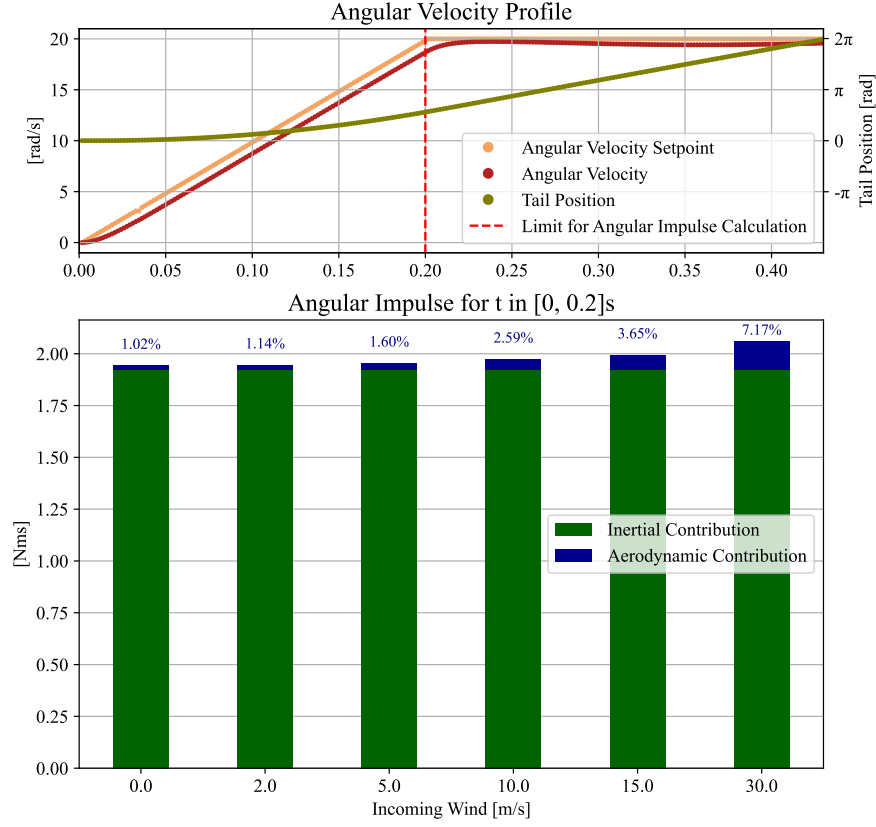


Figure 3.2: Top: Angular velocity, velocity setpoint and tail position. The red dotted line is at 0.2s, which is the upper limit used to integrate the angular impulse. Bottom: Bar plot for varying incoming wind speeds along the x-axis. In green the inertial contribution is shown, while the blue bar represents the aerodynamic contribution to the total angular impulse. The percentage of aerodynamic contribution is shown above the bar.

tion increases too.

The inertial contribution remains constant across all simulations. This is because the same acceleration profile is used for all simulations. The inertial torque T_{inertia} depends solely on the acceleration, e.g. $T_{\text{inertia}} = \dot{\theta}I$, where $\dot{\theta}$ is the angular acceleration and I is the moment of inertia with respect to the rotation axis.

In conclusion, the aerodynamic drag forces contribute significantly (7.17%) at high hunting velocities, but decline rapidly with slower hunting speeds where the relative contribution quickly drops below 3%. It is important to note that the blue bar does not simply show a quadratic dependency on the incoming velocity. The blue bar is quadratically dependent on the relatively weighted contribution of \mathbf{v}_{Wind} to \mathbf{v}_{Rot} , as shown in eq. (2.5) and eq. (2.2). However, as the incoming wind \mathbf{v}_{Wind} increases and becomes more dominant over \mathbf{v}_{Rot} , the more the aerodynamic contribution (blue bar in fig. 3.2) scales *approximately* with $\mathbf{v}_{\text{Wind}}^2$.

Chapter 4

Conclusion

This project explores the implementation of aerodynamic drag forces into the Nvidia Isaac Sim / Isaac Lab [1] framework using the hunting cheetah and aerodynamic roll torque contribution as a case study.

On the simulation front, it is shown how an analytical approach is used to calculate drag forces for a simple robot model (section 2.1) and applying a substitution force in simulation.

Another method for simulating drag forces using Nvidia’s Omniverse extension ”Force Fields” [2] is used and compared to the analytical approach. Despite both simulation methods providing similar results, the reason for the difference between the two methods is unknown at this time.

The analytical approach suffers mainly from the non generalizability of the code used for these simulations. For any other robot configuration, the specific aerodynamic drag effects would have to be considered and implemented. Given the general applicability benefit of using the force fields extension to simulate drag forces, this is for the time being considered the preferred method.

However, opposed to the analytical approach, the force fields approach requires the base of the robot to move through space, to create the notion of incoming wind. Depending on the research question at hand, specifically for robots that require ground interaction, this approach is unfeasible to simulate incoming wind.

The main takeaway from the case study is the aerodynamic roll torque contribution, neatly summarized as the angular impulse in section 3.2. It can be concluded that the aerodynamic contribution is relevant at high hunting speeds, 7.17 % at 30 m/s, and quickly drops below 3 % at lower speeds, despite having a fast tail-flicking motion (details in section 2.4.1).

For any aerodynamic simulation one must have a solid foundation, upon which the simulation parameters are chosen. The case study presented here relies heavily on the data provided by Patel, without it the choice for realistic cheetah tail parameters would not have been possible.

Chapter 5

Outlook

To pinpoint the precise difference between the analytical or the force fields approach, a simulation of a robot with real world experiments could provide the validation for either approach presented.

The force fields methodology should be prioritized as it's general applicability to a multi DoF robot is provided inherently. One could take a closer look at the precise implementation and potentially extend the framework to allow constant velocity offsets, allowing simulations with incoming wind without moving the base of the robot.

Both presented methods now enable robot simulations which consider aerodynamic drag. Through a broad-based simulation study, a multitude of design choices for aerodynamic appendages in robots can be evaluated prior to prototyping.

This could be used as a framework to optimize (aerodynamic) tail design, given a specific control objective.

On the biomechanics side, this framework provides a general methodology to simulate a variety of aerodynamic appendages. In nature, the cheetah is only one of many animals that are guessed to make use of the aerodynamic drag forces. The question of aerodynamic contribution can of course be extended in the case of the cheetah to more complex tail maneuvers, or extended to other species, potentially with larger tails, boasting a more significant drag force.

Bibliography

- [1] M. Mittal, C. Yu, Q. Yu, J. Liu, N. Rudin, D. Hoeller, J. L. Yuan, R. Singh, Y. Guo, H. Mazhar, A. Mandlekar, B. Babich, G. State, M. Hutter, and A. Garg, “Orbit: A unified simulation framework for interactive robot learning environments,” *IEEE Robotics and Automation Letters*, vol. 8, no. 6, pp. 3740–3747, 2023.
- [2] NVIDIA Omniverse, “Omniverse Force Fields Extension Documentation,” 2023, [Accessed: 06-Oct-2024].
- [3] R. Siddall, V. Ibanez, G. Byrnes, R. J. Full, and A. Jusufi, “Mechanisms for mid-air reorientation using tail rotation in gliding geckos,” *Integrative and Comparative Biology*, vol. 61, pp. 478–490, 8 2021.
- [4] A. Patel, E. Boje, C. Fisher, L. Louis, and E. Lane, “Quasi-steady state aerodynamics of the cheetah tail,” *Biology Open*, vol. 5, pp. 1072–1076, 8 2016, simulation of Cheetah Tail torques using values from wind tunnel tests (Cd value, flick speeds from video recordings).
- [5] S. W. Heim, in Zurich, M. Ajallooeian, P. Eckert, M. Vespignani, and A. J. Ijspeert, “On designing an active tail for legged robots: simplifying control via decoupling of control objectives.”
- [6] R. Briggs and J. H. Lienhard, “Tail use in bioinspired quadrupedal locomotion archives massachusetts institute of technology,” 2012.
- [7] D. Bright, S. Shield, and A. Patel, “Aerodima: Cheetah-inspired aerodynamic tail design for rapid maneuverability.”
- [8] BBC, “Cheetah hunting,” [Accessed: 10-Oct-2024].
- [9] Wikipedia, “Vector projection,” [Accessed: 11-Oct-2024].

Appendix A

Projected Surface Area

The fig. A.1 is used to explain the notion of L_{proj} and why it must be considered in the general case but can be neglected under certain conditions.

The figure A.1 shows on the left the tail (body not shown) with the vectors $\mathbf{v}_{\text{Rot}}(s)$ and $\boldsymbol{\omega}$ as already introduced and used throughout this project. The incoming wind \mathbf{v}_{Wind} acts parallel to the rotation vector $\boldsymbol{\omega}$. To get the total wind perceived $\mathbf{v}(s)$ along the tail, $\mathbf{v}_{\text{Rot}}(s)$ is added with \mathbf{v}_{Wind} (eq. (2.5)). From this it is clear that $\mathbf{v}(s)$ lies in the plane E spanned by the two addends. Due to the geometric nature of the vectors $\mathbf{v}_{\text{Rot}}(s)$, \mathbf{v}_{Wind} and $\mathbf{x}(s)$, providing an orthogonal basis, it is clear that the plane E is perfectly perpendicular to $\mathbf{x}(s)$. This holds for all timesteps and tial positions, assuming \mathbf{v}_{Wind} acts along $\boldsymbol{\omega}$.

The drag model (eq. (2.1)) requires the surface area A to be perfectly perpendicular to the incoming wind. As this is not always guaranteed, the surface area A can be projected to a plane, so that it is indeed perpendicular to the incoming wind, e.g. $A_{\perp \mathbf{v}(s)}$.

For the situation on the left, we have the total wind $\mathbf{v}(s) \in E$, while $E \perp \mathbf{x}(s)$. Due to the perpendicular nature of $\mathbf{v}(s) \perp \mathbf{x}(s)$, projecting the cylinder onto $F_{\perp \mathbf{v}(s)}$ gives a surface area of $A = A_{\perp \mathbf{v}(s)} = Ld$, where L is the tail's length and d the diameter.

The figure on the right shows the tail and the vectors $\mathbf{v}_{\text{Rot}}(s)$ and $\boldsymbol{\omega}$. As opposed to the left side of the figure, \mathbf{v}_{Wind} is *not parallel* to $\boldsymbol{\omega}$. To visually show this, the plane E from the left side is copied and shown in the right figure. The dotted lines under $\mathbf{v}(s)$ and \mathbf{v}_{Wind} are projection lines of the vectors onto the plane E . For a given $\mathbf{v}(s)$, the surface area perpendicular to it is given by $F_{\perp \mathbf{v}(s)}$, which for the general case shown is not aligned with the cylinder's longitudinal axis $\mathbf{x}(s)$. The plane $F_{\perp \mathbf{v}(s)}$ is used as a projection plane to derive the projected surface area $A_{\perp \mathbf{v}(s)}$.

Due to the nature of working with a cylinder, when projecting onto $F_{\perp \mathbf{v}(s)}$, only the the length-dimension of the cylinder L needs to be considered, e.g. $A_{\perp \mathbf{v}(s)} = L_{\text{proj}} d$. The diameter remains $d = d_{\text{proj}}$ independent of the plane projecting onto.

The projected length can be calculated using eq. (A.1). This equation takes the vector $\mathbf{x}(s) \Big|_{s=L}$ and subtracts the part of that vector which is parallel to

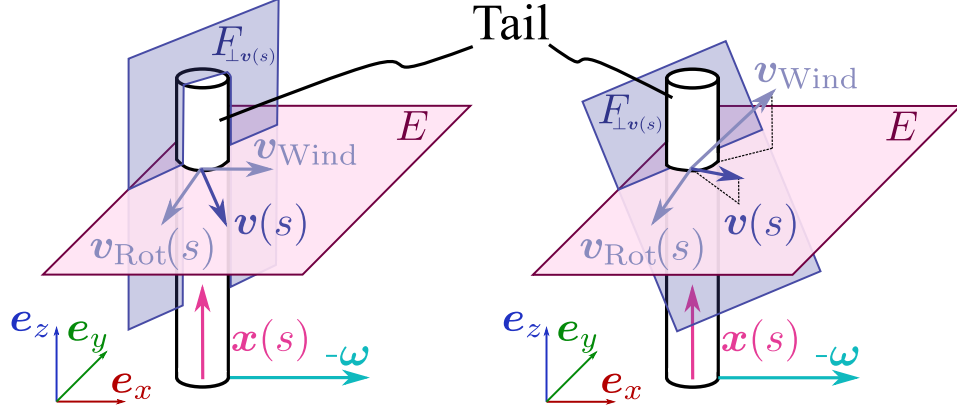


Figure A.1: This figure is used to explain the concept of projecting the surface area onto the plane $F_{\perp \mathbf{v}(s)}$ which is perpendicular to the total experienced wind $\mathbf{v}(s)$ at a point s along the tail. Note that the rotation vector $\boldsymbol{\omega}$ has a negative sign, as to have the velocities facing the viewer, making sketching easier. Left is the special case, where \mathbf{v}_{Wind} is parallel to the rotation axis $\boldsymbol{\omega}$, and the projected surface area is simply the "regular" surface area $A = Ld$. The plane E is spanned by the two vectors \mathbf{v}_{Wind} and $\mathbf{v}_{\text{Rot}}(s)$. On the right hand side is the special case, where \mathbf{v}_{Wind} is not parallel to $\boldsymbol{\omega}$. Hence, the $F_{\perp \mathbf{v}(s)}$ is not aligned with the cylinder's longitudinal axis $\mathbf{x}(s)$. To better visualize that \mathbf{v}_{Wind} is not parallel to $\boldsymbol{\omega}$, the plane E from the left figure is copied and shown in the right figure. The dotted lines show the projections onto the plane E . Figure is not to scale.

$\mathbf{v}(s)$, leaving only the perpendicular part. The the parallel component to $\mathbf{v}(s)$ can be extracted using the projection of $\mathbf{x}(s) \Big|_{s=L}$ onto $\mathbf{v}(s)$. The projection itself can be split into two parts; (1) scalar product between the vector in question $\mathbf{x}(s)$ and a unitary direction vector $\mathbf{e}_{\mathbf{v}(s)}$, providing a scalar value and then (2) multiplying by the unitary direction vector $\mathbf{e}_{\mathbf{v}(s)}$ [9].

$$L_{\text{proj}} = \left\| \mathbf{x}(s) - \underbrace{(\mathbf{x}(s) \cdot \mathbf{e}_{\mathbf{v}(s)}) \mathbf{e}_{\mathbf{v}(s)}}_{\text{Projection of } \mathbf{x}(s) \text{ onto } \mathbf{v}(s)} \right\|_{s=L} \quad (\text{A.1})$$

From this notion, we can derive the infinitesimal surface area A_{Δ} , which is required for the calculations elaborated in section 2.2. The derivation is shown in eq. (2.6), where we enforce that the integral of A_{Δ} is equal to the total surface area $A_{\perp \mathbf{v}(s)}$. The infinitesimal surface area for the general case is given by $A_{\Delta} = \frac{L_{\text{proj}}}{L}$.

Appendix B

Angular Velocity Tracking

As elaborated in 2.4.1, the tracked velocities might differ slightly between different simulation parameters. The figures provided here are for sake of completeness and to provide the reader with the option to make up their own mind, on whether these differences are relevant or not.

As per the evaluation done in context of this thesis, the differences are negligible.

Figure B.1 provides absolute maximum difference, mean difference and standard deviation between all angular velocities of all simulations used in the section 3.1, where the analytical method is compared to the force fields extension.

Figures B.2, B.3 and B.4 provide the same statistics for all runs from the section 3.2, where the effect on the angular impulse is analyzed. Remember that this experiment is conducted using the force field approach only.

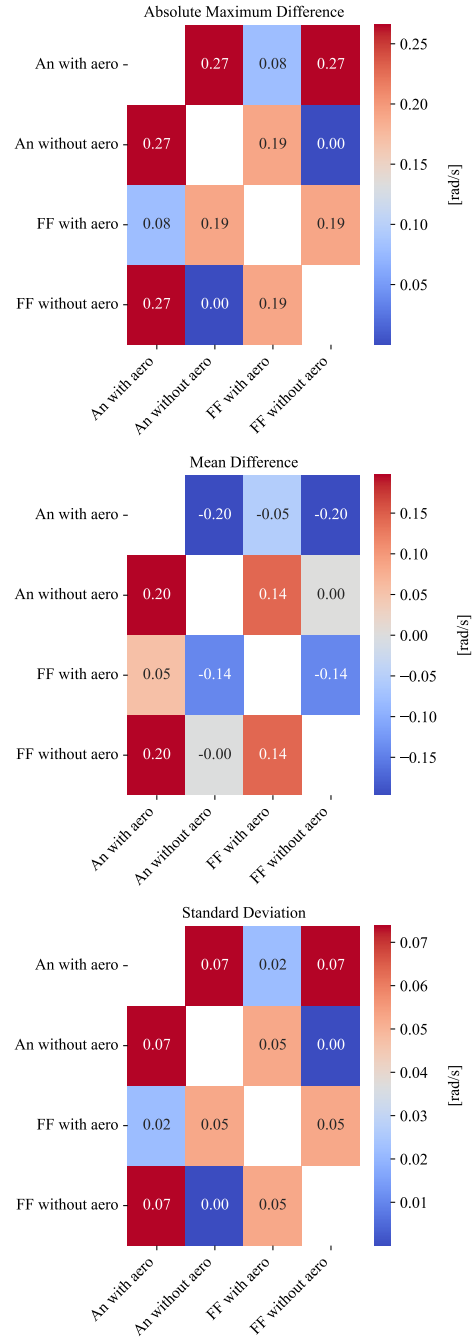


Figure B.1: Each figure provides a different statistical value computed based on the difference between two angular velocities. A short description of the simulation is given by the axis x and y. "An" Analytical method, "FF" Force Fields method, "with aero" and "without aero" refer to whether the simulation was run with aerodynamic drag or without.

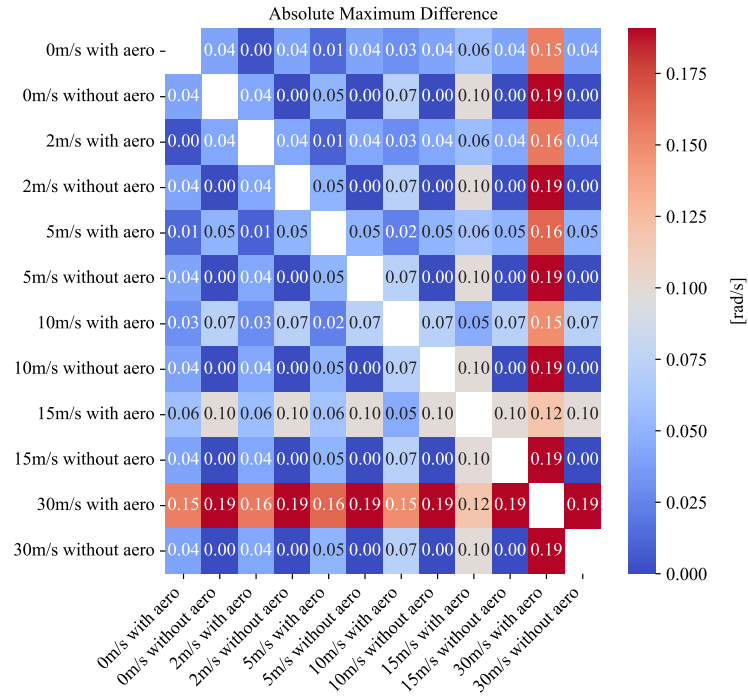


Figure B.2: Absolute maximum difference in angular velocity between all simulations with varying parameters. The incoming wind velocity is varied from 0 m/s until 30 m/s, while "with aero" and "without aero" indicate whether aerodynamic drag was enabled or not.

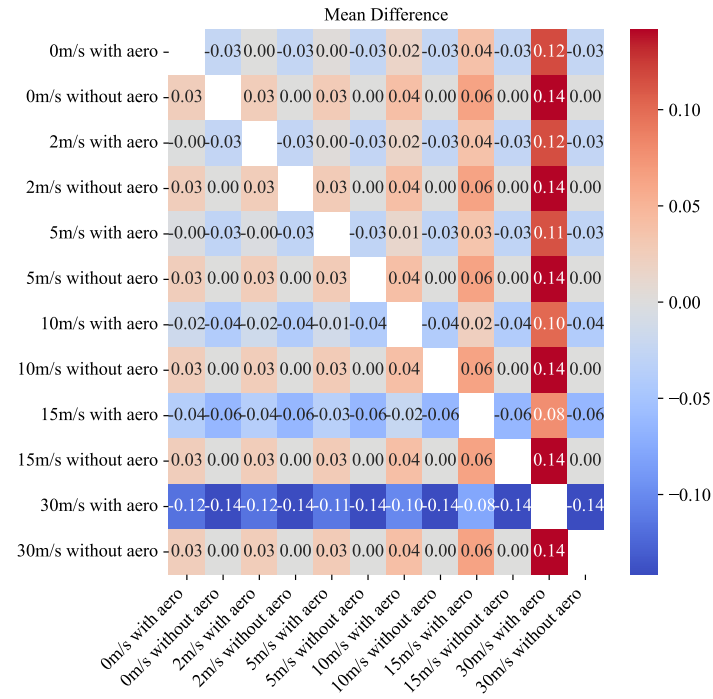


Figure B.3: Mean difference in angular velocity between all simulations with varying parameters. The incoming wind velocity is varied from 0 m/s until 30 m/s, while "with aero" and "without aero" indicate whether aerodynamic drag was enabled or not.

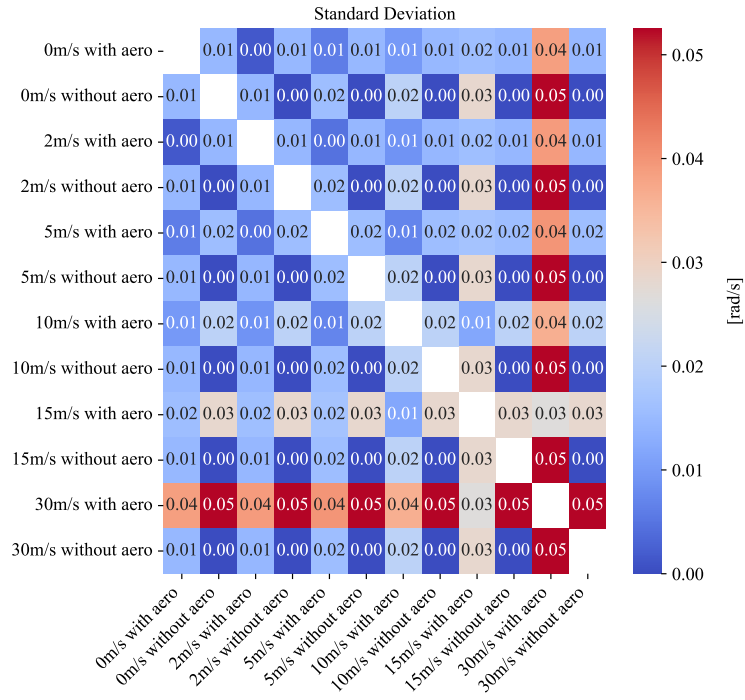


Figure B.4: Standard deviation of the difference in angular velocity between all simulations with varying parameters. The incoming wind velocity is varied from 0 m/s until 30 m/s, while "with aero" and "without aero" indicate whether aerodynamic drag was enabled or not.

